SANDIA REPORT

SAND2011-6814
Unlimited Release
Printed September 2011

Time Encoded Radiation Imaging

Peter A Marleau
Erik Brubaker
Mark Gerling
Aaron Nowack
Patricia F Schuster
John T Steele

Prepared by
Sandia National Laboratories
Albuquerque, New Mexico 87185 and Livermore, California 94550

Sandia is a multiprogram laboratory operated by Sandia Corporation,
a Lockheed Martin Company, for the United States Department of Energy's
National Nuclear Security Administration under Contract DE-AC04-94AL85000.

Issued by Sandia National Laboratories, operated for the United States Department of Energy by Sandia Corporation.

Available to DOE and DOE contractors from
U.S. Department of Energy
Office of Scientific and Technical Information
P.O. Box 62
Oak Ridge, TN 37831

Telephone: (865) 576-8401
Facsimile: (865) 576-5728
E-Mail: reports@adonis.osti.gov
Online ordering: http://www.osti.gov/bridge

Available to the public from
U.S. Department of Commerce
National Technical Information Service
5285 Port Royal Rd.
Springfield, VA 22161

Telephone: (800) 553-6847
Facsimile: (703) 605-6900
E-Mail: orders@ntis.fedworld.gov
Online order: http://www.ntis.gov/help/ordermethods.asp?loc=7-4-0#online

SAND2011-6814
Unlimited Release
Printed September 2011

Time Encoded Radiation Imaging

Peter Marleau
Erik Brubaker
Mark Gerling
Patricia Schuster
John Steele
Radiation and Nuclear Detection Systems (8132)
Sandia National Laboratories
7011 East Avenue
Livermore, California 95651-MS9406

Abstract

Passive detection of special nuclear material (SNM) at long range or under heavy shielding can only be achieved by observing the penetrating neutral particles that it emits: gamma rays and neutrons in the MeV energy range. The ultimate SNM standoff detector system would have sensitivity to both gamma and neutron radiation, a large area and high efficiency to capture as many signal particles as possible, and good discrimination against background particles via directional and energy information. Designing such a system is a daunting task. Using time-modulated collimators could be a transformative technique leading to practical gamma-neutron imaging detector systems that are highly efficient with the potential to exhibit simultaneously high angular and energy resolution. A new technique using time encoding to make a compact, high efficiency imaging detector was conceived. Design considerations using Monte Carlo modeling and the construction and demonstration of a prototype imager are described.

CONTENTS

FIGURES

TABLES

NOMENCLATURE

dB	decibel
DOE	Department of Energy
FOV	Field of View
IAEA	International Atomic Energy Agency
MCNP	Monte Carlo N-Particle
PMT	Photomultiplier Tube
PRISM	Portable Rotating Imager using Self Modulation
PSD	Pulse Shape Discrimination
RMC	Rotating Modulation Collimator
ROC	Receiver Operating Characteristic
SNL	Sandia National Laboratories
SNM	Special Nuclear Material
URA	Uniformly Redundant Array

1. INTRODUCTION

Time-coded apertures were introduced as a technique for gamma ray imaging in medical detectors in the 1970s. Despite promising conclusions in these initial papers on the subject, time-coded apertures have not become a standard technique in medical imagers, possibly because of the difficulties presented by imaging in the near-field regime (1)(2).

Outside of medical imaging, there has been limited work on time-encoding radiation detectors. The Rotating Modulation Collimator (RMC) is the exception and has seen application in both astrophysics and security applications (3)(4)(5).

The RMC demonstrates several advantages of the time-encoding technique: imaging with a single non-position-sensitive detector, good angular resolution, and the absence of artifacts arising from un-attenuated background events. However, the RMC has a fundamentally limited field of view, as well as a geometrical efficiency that is lower than a typical 50% open coded aperture imager. Additionally, although an RMC sensitive to thermal neutrons has been investigated; fast neutrons are inherently unsuited to an RMC since the thick collimators needed to attenuate them would severely impact the RMC efficiency. We have pursued a more general application of time modulation to the SNM detection problem that is highly efficient, scalable, and applicable to fast neutron detection.

We have recently demonstrated coded aperture as well as time encoded imaging of fast neutrons using a rotating Uniformly Redundant Array (URA) mask (6)(7). In an ideal traditional (not time-encoding) coded aperture imager, a properly selected coded mask will provide artifact-free reconstruction (8). But non-uniformities, which induce reconstruction artifacts, are very difficult to suppress in a real system. The non-uniformities can arise either from variations in the background field at the image plane due to the local environment or the detector shielding configuration, or from variations in the detector calibrations. In this work we concluded that, by converting the spatial modulation of the signal to time modulation, the imaging performance of the ideal coded aperture can be maintained, while simplifying the system design and increasing robustness to local variations in the background field.

A simple conceptual detector was built to demonstrate the feasibility of a time-encoding collimator. Dubbed LIGHTHOUSE, this proof of concept imager comprises a single central detector, a 5” high, 5” diameter LOS filled aluminum cell coupled to a 5” PMT placed at the center of a series of mask bars arranged in a URA pattern and wrapped into a circle. Figure 1 shows the geometry as simulated and built. The mask is arranged in a 31 element URA pattern and constructed from 3.5”×3.5”×27” high density polyethylene bars. The neutron modulation as a function of angular position can be seen in Figure 2 (right). Figure 2 (left) shows the results of the application of a Maximum Likelihood (MLEM) (9) imaging reconstruction technique described.

For this demonstration, little was done to optimize the design. It was essentially constructed from what was available at the time. In this work we took this concept beyond a simple proof of feasibility with careful modeling and simulations.

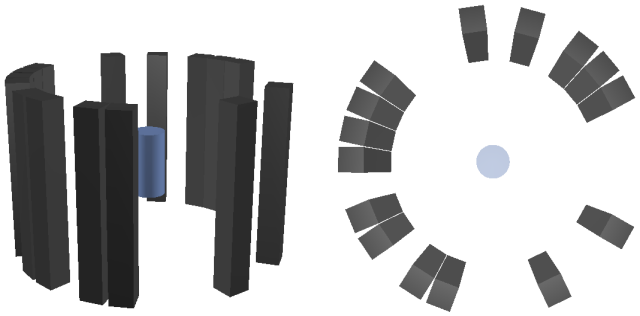

Figure 1: Side view (left) and top view (right) of the time encoded imager used in simulations.

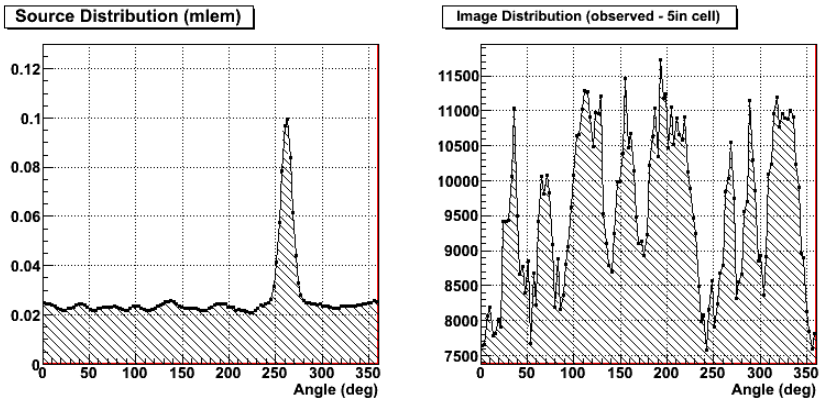

Figure 2: Neutron counts as a function of azimuth angle (arbitrary phase) of the 5" diameter detector (right) and the result of an MLEM image reconstruction (left) (vertical axis is in neutrons per second).

1.1. The PRISM concept

The concept for this work was originally intended to extend the proof of concept described in the previous section to create a larger and more efficient "LIGHTHOUSE" type imager. The target application is to detect and locate special nuclear material (SNM) at large stand-off distances. Toward this goal, we designed a very large central detector (22 inches diameter x 22 inches depth). However, it was quickly realized that portability constraints would greatly limit the performance of such a detector. In order to fit a rotating mask into a transportable container of reasonable size (~8 feet across), the number of mask elements that encircle the central detector would need to be constrained to achieve an aperture size comparable to the large diameter of the central detector, constraining the angular resolution of the imager. In addition, the mass of a rotating mask this size would lead to some engineering challenges. In summary, though applications certainly exist where this concept is appropriate, a scaled up version of LIGHTHOUSE was proving to be less than practical.

Therefore, we created a new concept based on time encoded imaging that does not require large masses of shielding material. The Portable Rotating Imager using Self Modulation (PRISM) is

comprised of only a few detectors that rotate around each other on a common axis. Because the material of adjacent detectors is used to attenuate the signal in any one detector there is no need for the large amounts of extra material required for the LIGHTHOUSE mask. The footprint and overall mass of the imager is thus reduced to the size and mass of the detectors alone.

This leads to a much more efficient and compact imager, however the imaging properties of the URA mask are lost. There is no longer a mathematical guarantee that a point source will reconstruct with little or no artifact, but this design allows for much more detector material in the volume allotted to the imager. Thus for the same dwell time, the PRISM detector will collect greater statistics which may overcome its lack in image quality on a per event basis. All of these factors inspired us to design and construct a number of large liquid scintillator detectors to field in a large stand-off demonstration.

1.1.1. Detector Design

Due to funding limitations we attempted to make use of the resources available whenever possible. Four 9 inch photomultiplier tubes (PMTs) that were previously used in a decommissioned antineutrino detector were repurposed for use in this project. Therefore we designed our detectors around this constraint. A 12" diameter steel can was built to hold an assembly that holds each PMT in direct contact with ~27 liters of liquid organic scintillator EJ-309 (Eljen) 15" above the bottom of the can. A small argon filled expansion chamber above the PMT holder (seen in Figure 3) allows the scintillator to expand with temperature as well as providing a place for excess scintillator to move as the detectors rotate without changing the active detector volume. The assembly is held into place with a piston that is sealed airtight with double o-rings. The end of the PMT is passed through the piston and sealed with a third o-ring so that the electronic signal can be passed out through the base and high voltage passed in through the voltage divider. The entire assembly is then made light tight with a lid that bolts down onto the top of the piston.

The signals from the 4 detectors are digitized by an SIS3350 4 channel 500 Megasample/second 12-bit digtizer card (10) and read out to a Windows PC using custom data acquisition software.

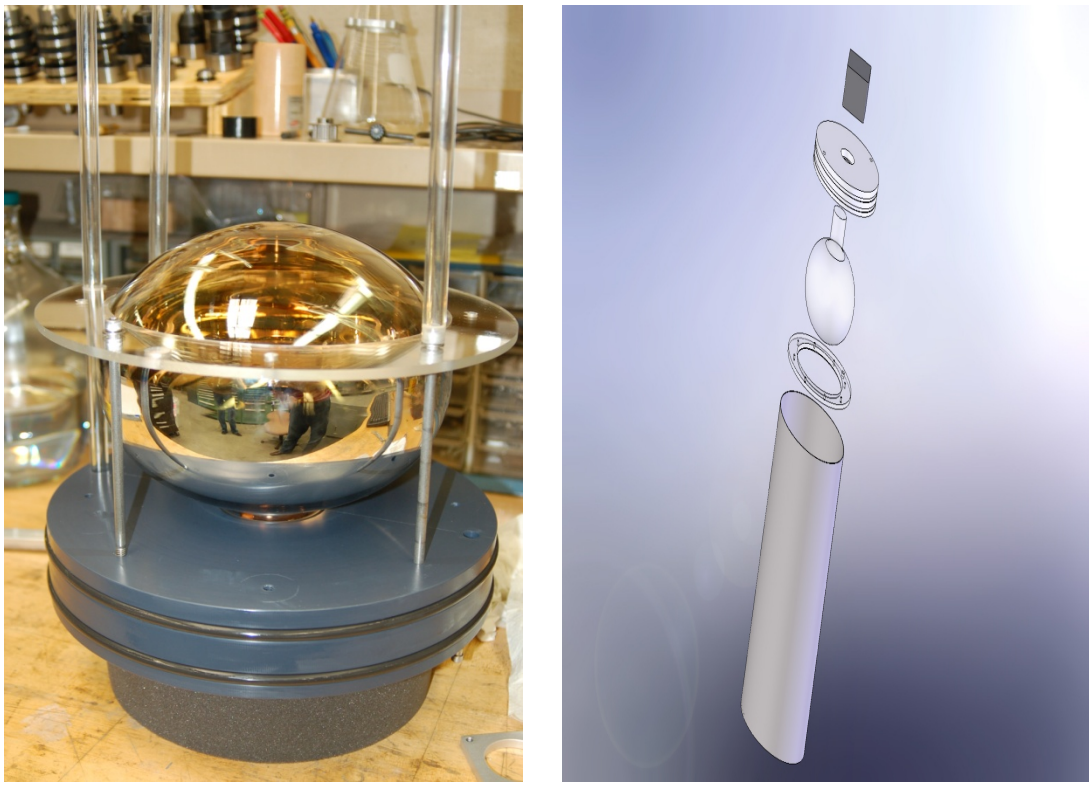

Figure 3: (left) Photograph of the PMT assembly before insertion into the liquid scintillator cell. (right) Exploded view of the design of the liquid scintillator cell showing the steel can, PMT holder, PMT, piston with o-ring seal and PMT base.

Four detectors were assembled and tested. Each exhibited excellent detection response and pulse shape discrimination (PSD). The physical cross-sectional area presented to an SNM source from the side of a single fully assembled cell is ~1160 cm^2, and Monte Carlo simulations indicate that even with reasonable assumptions about the minimum energy detection threshold (160 keV electron equivalent), a fission neutron efficiency of greater than 90% might be expected. However, once inefficiencies due to analysis cuts on PSD are introduced the true efficiency is likely to be lower.

2. SOFTWARE AND SIMULATION

The base detector unit is described in Section 1. This Section describes the optimization of the geometry and orientation of these detectors to provide the best detection and imaging performance in the PRISM concept. We have built software tools to simulate and analyze the PRISM detector system. The overall structure of the software is built in Python, a programming language which is useful for text file manipulation and plotting functions. We use MCNP-PoliMi, a widely used and validated code for detector physics, to model the detectors and perform the physics calculations (11). To analyze detector system performance, we use previously developed software based in ROOT (12) to create Receiver Operating Characteristic (ROC) curves.

The software package has been designed so that the user has to modify a minimal number of parameters between runs. As shown in Figure 4, the Python script takes in an MCNP template input file and run parameters specific to that run, and performs all operations to write the MCNP input files, run then, and extract the results. The final product for the process shown in Figure 4 is an observation map, which is a plot of signal to a given detector as a function of rotation angle.

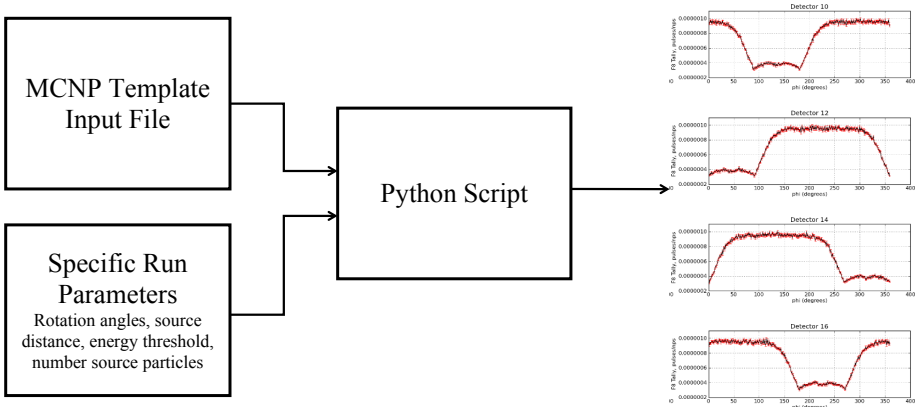

Figure 4: Diagram showing the input and output that the user sees while using the software package.

Figure 5 shows observation maps for single interactions in detector 1 and double interactions that interact first in detector 2 and second in detector 1. In this example the singles observation map shows that detector 1 receives a fairly constant signal when it is on the side of the system closest to the source. The two dips in detector signal occur when detector 1 is on the farther side from the source, and detector 3 blocks detector 1, and then detector 2 blocks detector 1. In this way we have created a self-shielded modulating system. The pattern of variation in the observation map is unique to each detector system and is important to determining where the source is. By modifying the detector system, we can adjust the observation map to try to improve the system performance.

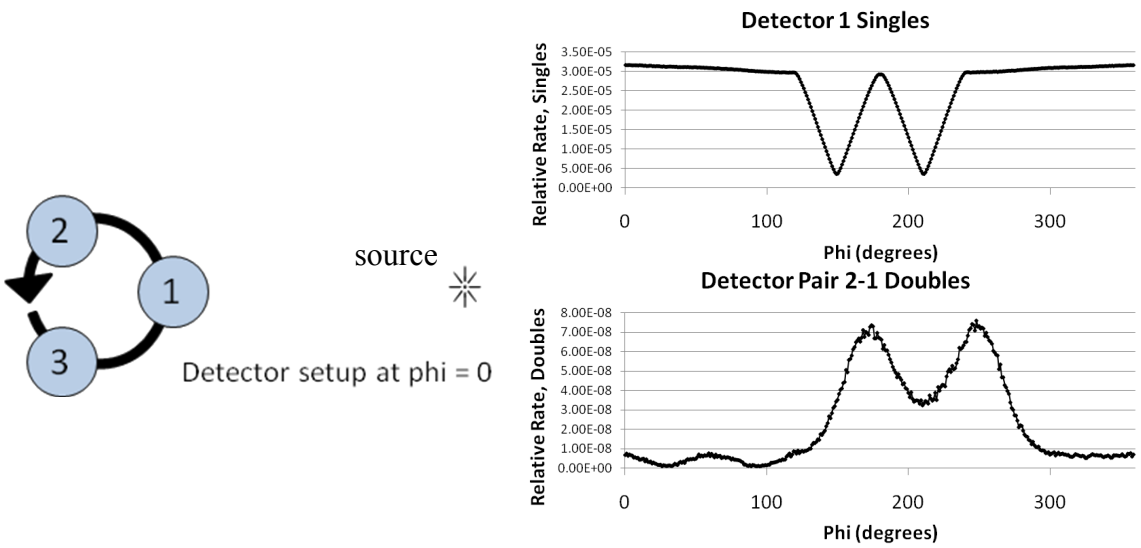

Figure 5: Observation maps for single interactions in detector 1 and double interactions from detector 2 to detector 1 for the detector setup shown.

The doubles interaction observation map shown in Figure 5 shows how the frequency of double interactions from detector 2 into detector 1 vary as a function of phi. For this, the signal is fairly constant and low when detector 2 is on the far side of the system and detector 1 is closer to the source. During these times, it is difficult for a particle to reach detector 2 and then scatter back into detector 1. The region in this plot with higher rates occurs while detector 2 is closer to the source and detector 1 is behind it. The maxima occur when the vector from the source to detector 2 makes a 30 degree angle with the vector from detector 2 to detector 1 as expected from fast neutron kinematics. In Figure 5 a 5" diameter x 5" deep liquid scintillator cell was modeled. In this case there are ~400 times more single scatters than double scatters. Though this is a small percentage of the total signal, we found that adding this response to the image reconstruction helped improve the angular resolution of the detector.

In the case of the 12" diameter cells that were built for the demonstration, double scatters represented only ~1/4000 of the total data collected. This is due to a much larger probability for multiple scatters in a single detector. An incident neutron is likely to either be captured or loose enough energy through multiple interactions that it drops below the energy threshold of the other detectors. In any case, for the rest of this work the double interaction component of the measurements were not used for image reconstruction.

3. ROC CURVE ANALYSIS

We chose to use ROC curves as our primary means of comparing the performance of detector systems with different geometries and orientations. For scenarios characterized by a binary real state (source above background present or absent) and a corresponding binary detector output, ROC curves produce a graphical plot of sensitivity, plotting the true positive rate vs. the false positive rate that allows for the immediate visualization of detector performance as some threshold parameter is varied. A curve that passes through the point (0,1) indicates that there exists an operating point with perfect performance; all true positives and no false positive signals. A straight diagonal with slope 1 indicates that the system output does not depend on the presence or absence of a source, and thus is equivalent to an uninformed guess. An improved signal will stretch toward the perfect point as shown in Figure 6 with the curve marked "better." The farther this curves stretches toward the upper left, the better the performance.

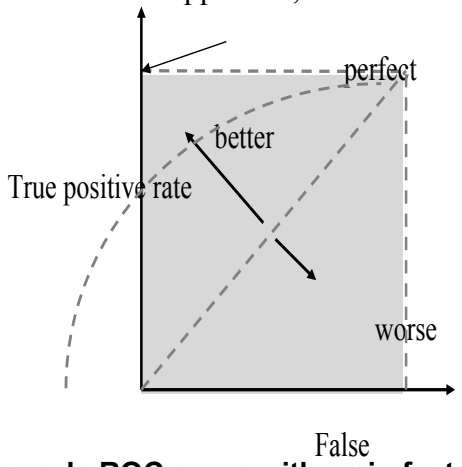

Figure 6: Example ROC curve with main features labeled

Our first analysis was performed to determine the optimum number of detectors and detector spacing for two PRISM detectors of different sizes. The "small" detectors are 5" tall and 5" in diameter and the large detectors are 15" tall and 12" in diameter (as described in Section 1).

In order to compare given detector systems, we chose scenarios (count time, source strength, and background rate) that produced ROC curves in a region somewhere between perfect and diagonal. As long as the detector systems we are comparing have the same count time, source strength, and background strength, the ROC curve will provide a reliable comparison of the two systems.

For the large detectors the scenario parameters were for a quantity of weapons grade plutonium deemed significant by the IAEA (13) at a distance of 60 meters and a 72 second dwell time. The same source and distance were used for the small detectors but the dwell time was adjusted to 540 seconds. The fast neutron background rates were estimated from the effective areas calculated from MCNP (14) averaged over the fission spectrum (spectrally similar to background) and an average isotropic flux of 5.0e-3 neutrons/second/cm2 between 0.5 and 10 MeV.

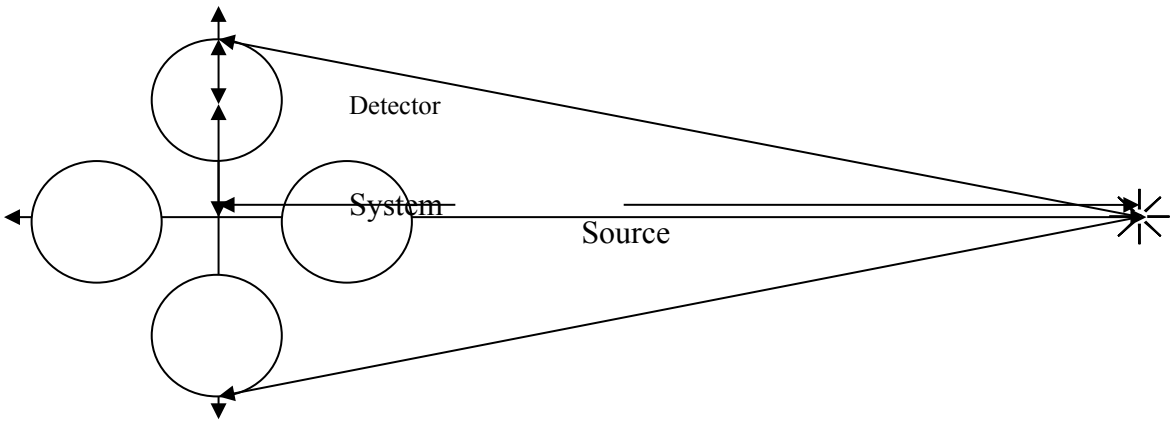

Figure 7: Diagram of the PRISM detector setup, viewed from above, as simulated in MCNP with measurements labeled by name.

Figure 7 shows a diagram of the PRISM detector setup, viewed from above, with dimensions labeled by name. We studied configurations with 3 and 4 detectors, and varied detector spacing by adjusting the system radius. The smallest system radius was chosen so that the active detector volume was right up against the next detector, and the maximum system radius was equal to 1.5 times the detector radius.

Figure 8 shows an example of a background (top) and source plus background (bottom) simulation. The source distributions shown on the left are used as input into detector response models. One-thousand data sets are generated from each of these distributions using the observation maps described above. MLEM reconstruction algorithms are then used on these data sets to generate images. The maximum value of the image is saved for each of the two-thousand runs. Finally, ROC curves are generated using a threshold on the maximum value as an alarm criterion. As a threshold is varied, the false positive rate is calculated as the fraction of background maxima that cross the threshold and the efficiency is calculated as the fraction of source plus background maxima that cross the threshold.

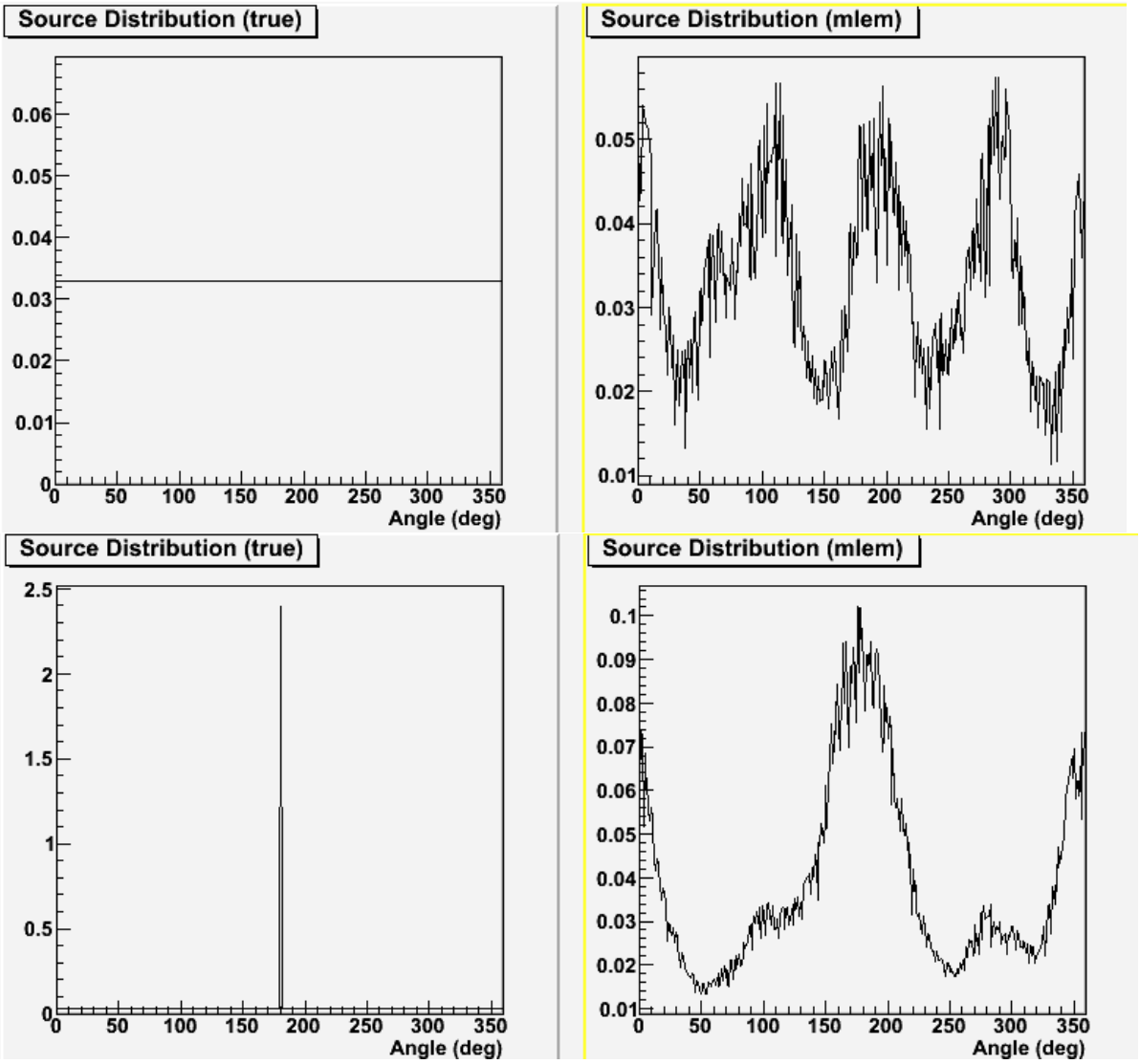

Figure 8: Examples of the true source distributions used in the ROC curve analysis (left) and the corresponding MLEM reconstructed images (right) for background only (top) and source plus background (bottom).

First, to compare the spacing of the detectors, we plot the same detector system at various system radii on the same axis. The axis label includes the number, size, and system radius of the detectors. For instance, the curve labeled "ROC_3L17_7808" in Figure 9 is a ROC curve for 3 large detectors at system radius 17.7808 cm (7 in.).

Figure 9 shows four plots that compare system performance for a given detector combination at various system radii. The four detector combinations are 3 small, 3 large, 4 small, and 4 large detectors. This figure shows that the detector systems perform best when the detectors are closest together at the smallest system radius. This is very clear for 3 small, 3 large, and 4 small detectors. For 4 large detectors, it does not make a strong enough difference to favor any system radius.

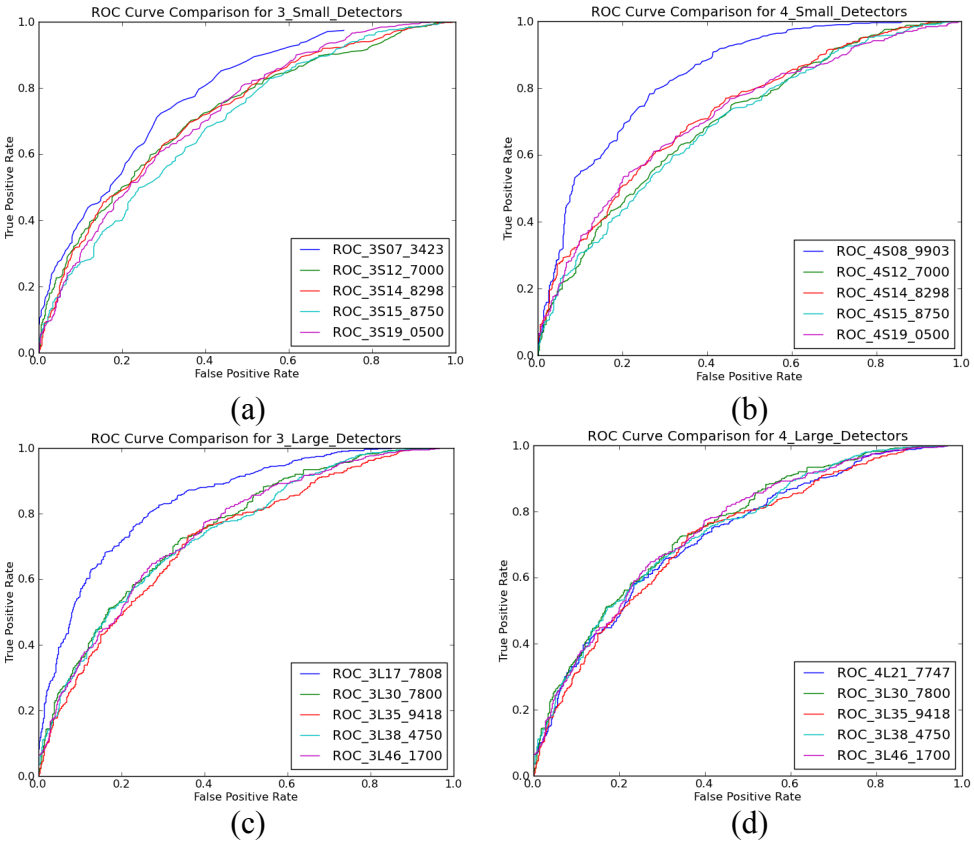

Figure 9: ROC Curves for PRISM detector systems with (a) 3 small detectors, (b) 4 small detectors, (c) 3 large detectors, and (d) 4 large detectors.

This is a surprising result because detector systems that are closer together have a smaller effective area than detector systems that are more spread out. Table 1 shows a list of effective areas as determined from Monte Carlo simulations for each detector configuration. Although a larger effective area means more total detected counts and better statistics, the ROC curves have shown that this does not necessarily lead to improved detection. This is most likely due to improved modulation as a function of rotation angle leading to better image quality and thus discrimination between source and background even with fewer events.

Table 1: Effective areas in cm^2 of the detector systems at various system radii.

System Radius	3 Small	4 Small	3 Large	4 Large
Pushed Together	309.6912	373.4662	2372.304	2807.191
Diameter	349.8284	416.9816	2852.978	3310.664
Diameter * 1.1677	357.0303	433.9044	2932.554	3512.115
Diameter * 1.25	359.9338	440.7002	2964.644	3573.514
Diameter * 1.5	366.9209	456.3141	3040.262	3743.036

Next we determine whether 3 or 4 detectors are best for small and large detector systems. Figure 10 displays the ROC curves for small and large detectors at the smallest system radius. This

figure shows that, for small detectors, it is better to have 4 detectors. For large detectors, it is better to have 3 detectors. This is a surprising result since 4 large detectors have a much higher projected area than 3 large detectors, as shown in Table 1. A 4-detector system would achieve a higher count rate due to its larger effective area, but again the ROC curve analysis suggests that improved image quality due to the modulation pattern of 3 detectors vs. 4 leads to better source detection.

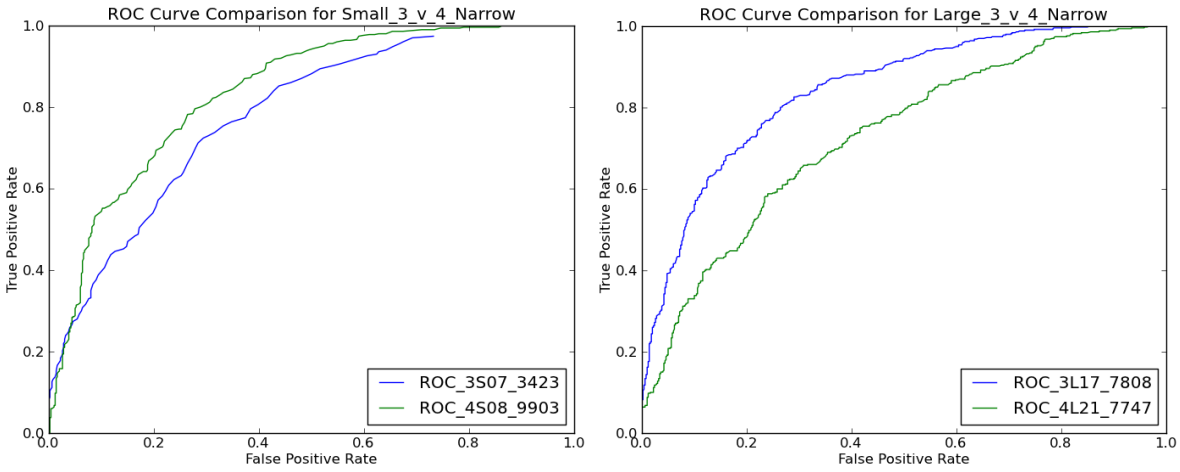

(a) (b)

Figure 10: ROC Curves for narrow PRISM detector systems with (a) small detectors and (b) large detectors.

4. DEMONSTRATION AND RESULTS

We have used the findings from the MCNP modeling described in the previous section to design an experimental setup of three large detectors in the lowest radius configuration. As seen in Figure 11 (left), the detectors were mounted to a turn table that is controlled by the data acquisition system by Ethernet. The drive motor includes a shaft encoder which is polled once per second to track the orientation of the detectors through the course of the measurements. The detectors were oscillated through +/- 190 degrees with a period of 360 seconds.

The detectors and turntable were installed inside the insulated and air-conditioned trailer seen in Figure 12 along with two other imaging systems (seen in Figure 11 (right)): the Neutron Scatter Camera and LIGHTHOUSE. The trailer was parked in the area outside the sewer outfall building in the north-west corner of Sandia National Laboratory California and a Cf-252 neutron source was positioned in several locations in the field to the east of the detectors as seen in Figure 13 and Figure 14.

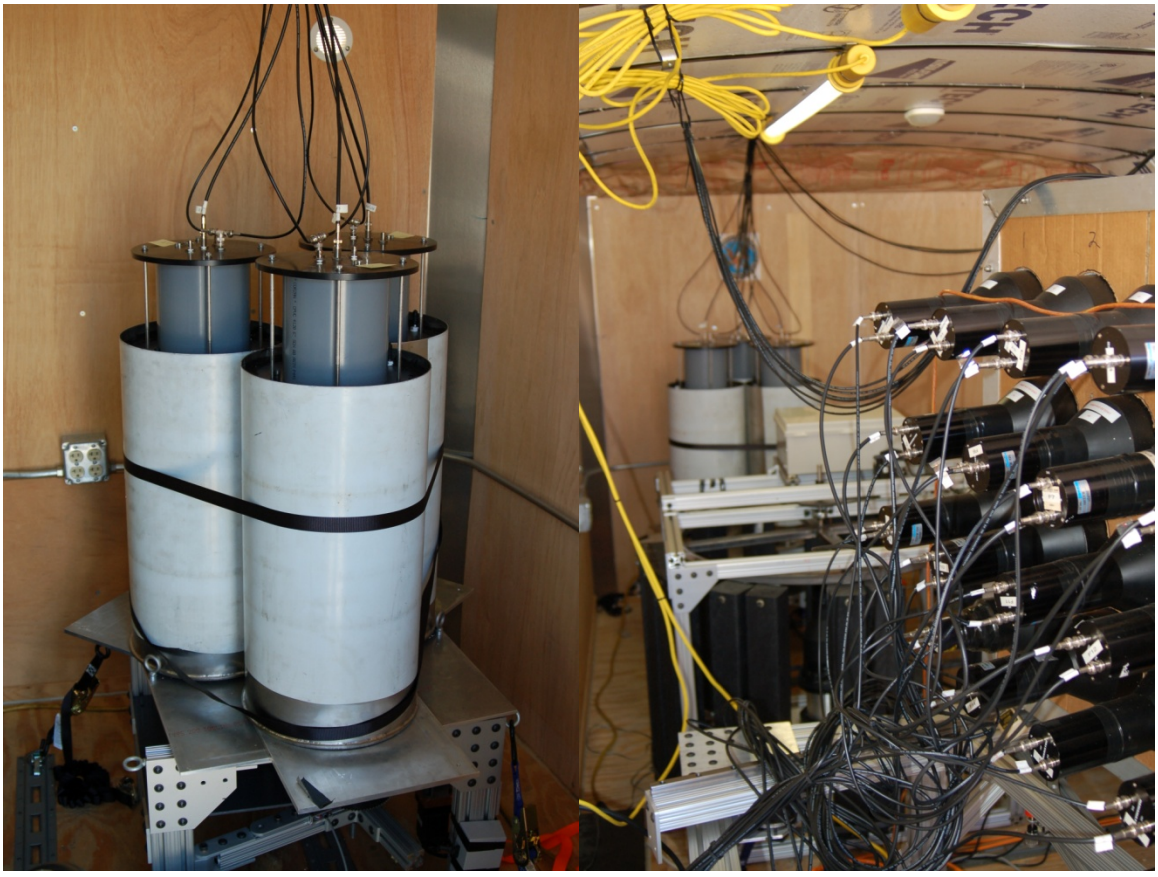

Figure 11: The three PRISM detectors mounted to the turn table (left). The three imaging systems installed in the trailer for this demonstration (right): neutron scatter camera (foreground), LIGHTHOUSE (middle ground), and PRISM (background).

Figure 12: Photograph of the trailer in which the three imaging systems were installed.

Figure 13: Top view of the sewer outfall building and surrounding area. Three of the source locations are marked as red dots and the detector trailer is marked as a grey box at the center of the 100 meter radius dotted circle. (Photograph taken from Google Maps(15)).

Figure 14: Photograph of the field in front of the detector trailer (left) and zoom region containing the source box.

In the first of several imaging demonstrations, a Cf252 neutron source with a neutron emission rate consistent with an IAEA significant quantity of weapons grade plutonium was positioned in three different locations in the field adjacent to the detector trailer. As seen in Figure 15, the source was positioned at a distance of 10 meters (35 feet) at positions approximately 50 degrees apart.

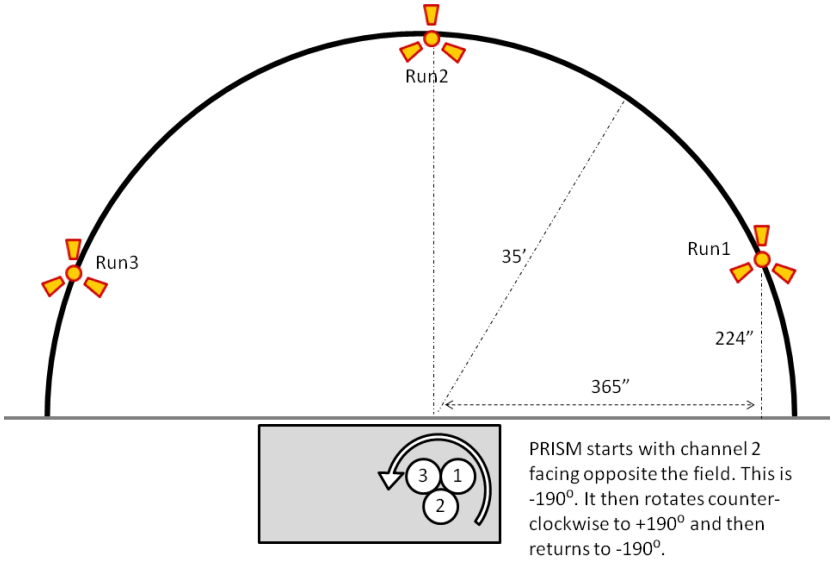

Figure 15: Illustration of the PRISM detector in the trailer (bottom) and the three locations of the Cf252 source.

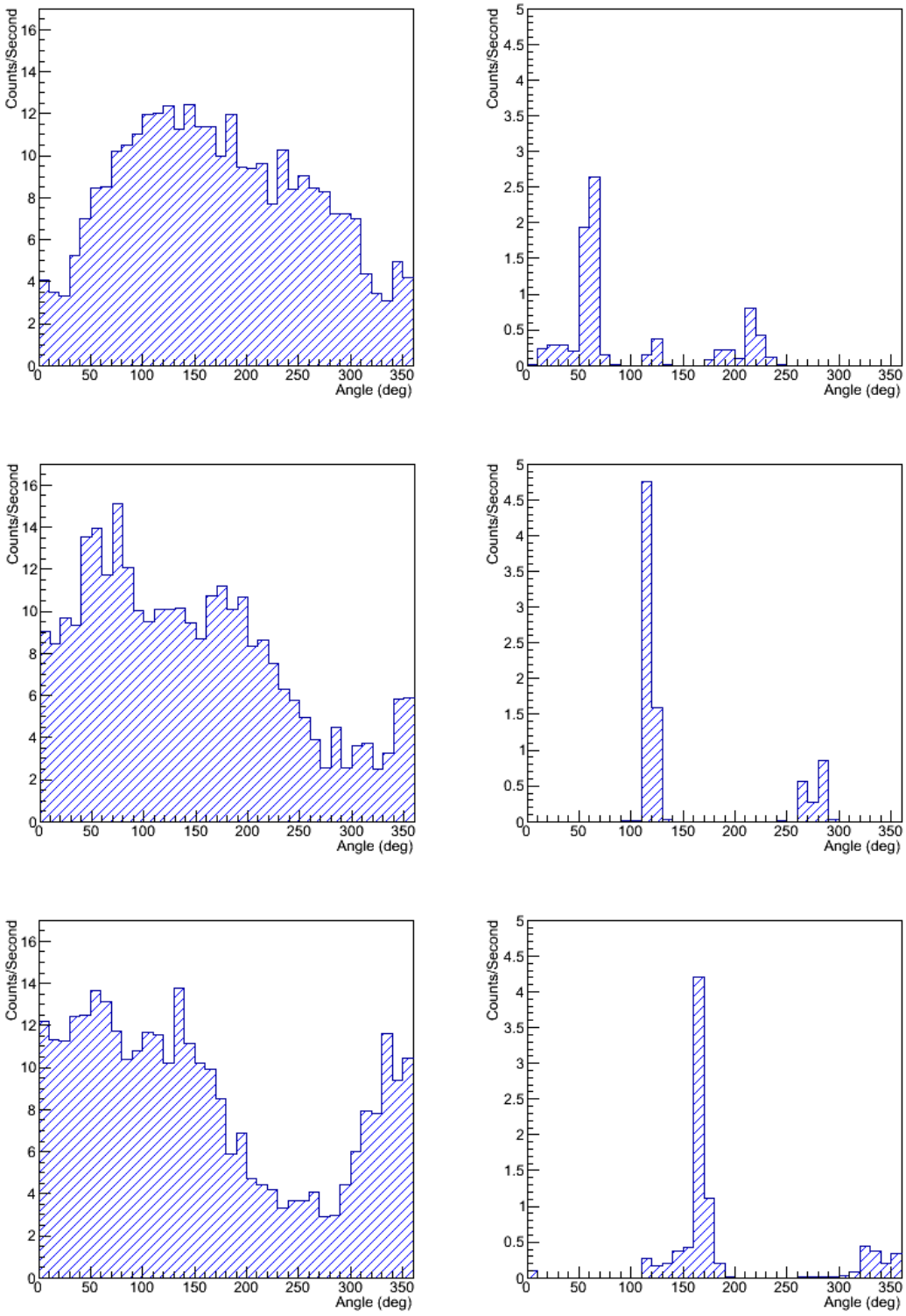

Figure 16: The measured neutron rates (left) and MLEM reconstructed rates (right) for the 3 source positions labeled Run 1 (top), Run 2 (middle), and Run3 (bottom) in Figure 15.

The measured counts per second in a single detector are shown in Figure 16 (left) and the MLEM reconstruction of the source distributions are shown in Figure 16 (right) for the three source positions shown in Figure 15. The modulation as a function of angle due to the attenuation of the other two detectors as they are rotated is readily apparent. These images indicate the presence of a point source in the appropriate locations; separated by 50 degrees as expected. Each run represents approximately 90 seconds of dwell time.

We next moved the source to positions at 60 meters and 100 meters distance as shown in Figure 13. The measured modulation is shown in Figure 17 (left) (total dwell time of 100 minutes at 60 meters and 130 minutes at 100 meters) and the reconstructed images are shown in Figure 17 (right). Again, the images indicate the presence of point sources at the expected angles.

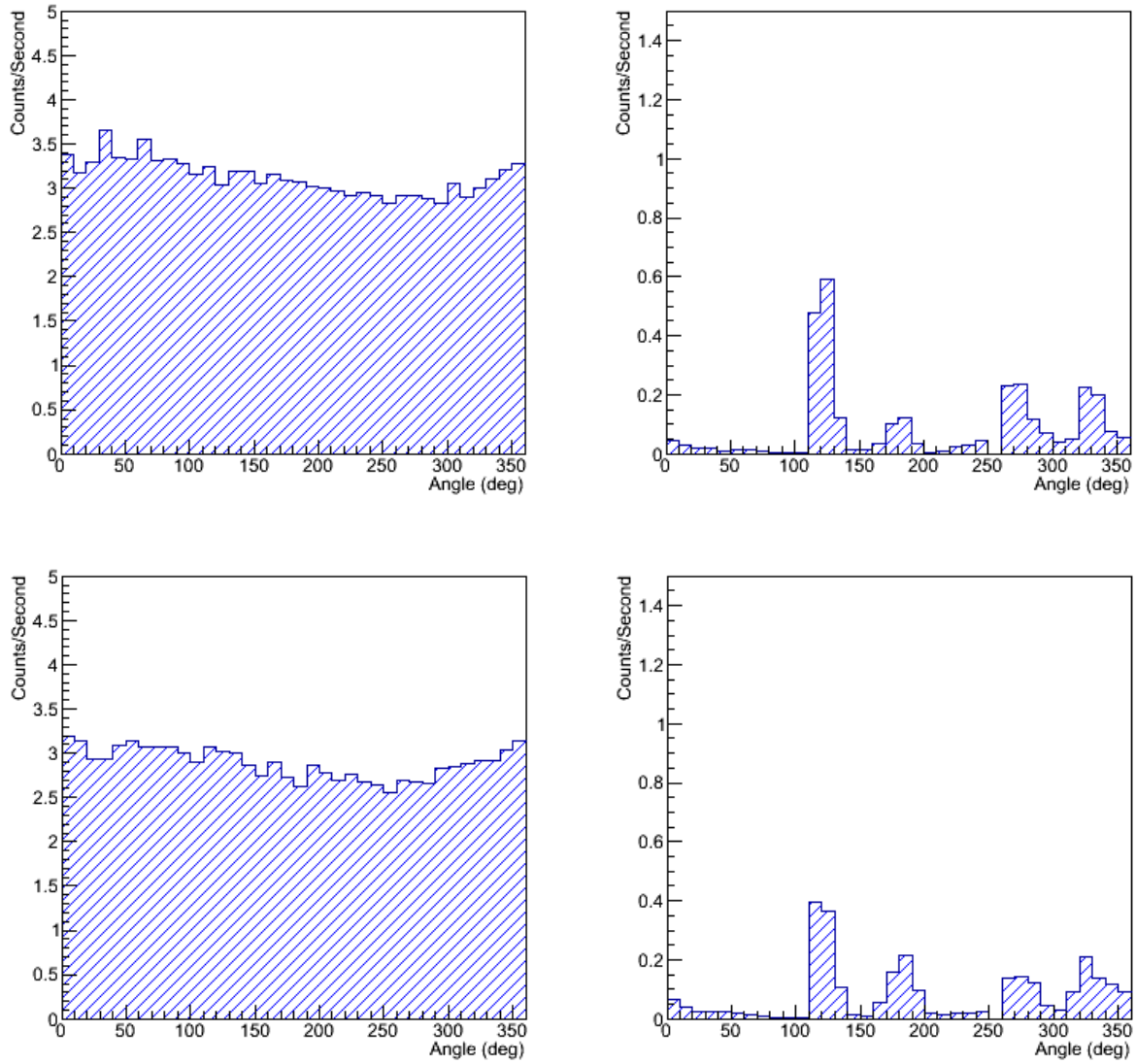

Figure 17: The measured neutron rates (left) and MLEM reconstructed rates (right) for a Cf252 neutron source at a stand-off of 60 meters (top) and 100 meters (bottom).

5. CONCLUSIONS

Through the use of Monte Carlo modeling and ROC curve analysis, we have carefully designed a prototype high efficiency fast neutron imager using the principles of time encoded imaging. The imager was built and integrated with a digital data acquisition system that allowed us to use variations in pulse shape to discriminate between fast neutron and gamma ray interactions. Modulation in the detected fast neutron rates as a function of the angular orientation of the detector due to the attenuation of neighboring detectors is used to reconstruct the neutron source distribution in 360 degrees around the imager.

The system was installed in a 20 foot trailer along with two other imaging systems and tested using a Cf252 neutron source as an SNM surrogate. The system successfully detected and imaged the source out to a stand-off distance of 100 meters. This first demonstration of this novel imaging technique illustrates the potential for this technology to be used in future SNM movement and detection applications.

[Blank page following section.]

6. REFERENCES

1. *Digital Tomographic Imaging with Time-Modulated Pseudorandom Coded Aperture and Anger Camera.* **Koral, Kenneth FW, Leslie Rogers, and Glenn F Knoll.** 5, 1974, Journal of Nuclear Medicine, Vol. 16, pp. 402-413.
2. *Gamma-Ray Imaging with Stochastic Apertures.* **May, Randall S, Ziya Akcasu, and Glenn F Knoll.** 11, 1974, Applied Optics, Vol. 13.
3. *The RHESSI imaging concept.* **Hurford, G J, E J Schmahl, R A Schwartz, A J Conway, M J Aschwanden, A Csillaghy, B R Dennis, et al.** 1-2, 2002, Solar Physics , Vol. 210.
4. *A rotating modulation imager for locating mid-range point sources.* **Kowash, B.R., D.K. Wehe, and J.A. Fessler.** 2, 2009, Nuclear Instruments and Methods in Physics Research Section A, Vol. 602.
5. *Thermal neutron imaging with a Rotationally Modulated Collimator (RMC).* **Boyce, Nathan O., Benjamin R. Kowash, and David K. Wehe.** Orlando : s.n., 2009. IEEE Nuclear Science Symposium. pp. 1129-1133.
6. *Active Coded Aperture Neutron Imaging.* **Marleau, P, et al.** 2009. IEEE NSS.
7. *Calibration and Simulation of a Coded Aperture Neutron Imaging System.* **Brubaker E, Marleau P, et al.** Orlando, FL : s.n., 2009. IEEE NSS.
8. *Coded aperture imaging with uniformly redundant arrays.* **Fenimore, E. E., and T. M. Cannon.** 3, 1978, Applied Optics, Vol. 17.
9. *Maximum likelihood reconstruction for emission tomography.* **Shepp, L A, and Y Vardi.** 2, 1982, IEEE transactions on medical imaging, Vol. 1, pp. 113-122.
10. **SIS.** SIS3350 data sheet. [Online] http://www.struck.de/sis3350.htm.
11. *MCNP-PoliMi: A Monte-Carlo code for correlation measurements.* **S. A. Pozzi, E. Padovani, and M. Marseguerra.** 3, November 11, 2003, Nuclear Instrumenation Methods in Physics Research A, Vol. 513, pp. 550-558.
12. *ROOT - An Object Oriented Data Analysis Framework.* **Rademakers, Rene Brun and Fons.** Lausanne : Nucl. Inst. & Meth. in Phys. Res. A, 1997. AIHENP'96 Workshop. Vol. 389, pp. 81-86.
13. *IAEA Safeguards Glossary.* **IAEA.** Vienna, Austria : International Verification, 2002, Vol. 3. Table-II and paragraph 3.14.
14. *Measurement of the flux and energy spectrum of cosmic-ray induced neutrons on the ground.* **Gordon, MS, et al.** 6, part 2, 2004, IEEE Transactions on Nuclear Science , Vol. 51.
15. **Google.** Map of Sandia National Lab, CA. *Google Maps.* [Online] http://www.maps.google.com.
16. **Eljen.** EJ-309 data sheet. [Online] http://www.eljentechnology.com/datasheets/EJ309%20data%20sheet.pdf.

[Blank page following section.]

DISTRIBUTION

1	MS9004	James Lund	8130
1	MS9004	Peter Davies	8100
1	MS9154	William Ballard	8200
1	MS9402	John Goldsmith	8132
1	MS9406	Peter Marleau	8132
1	MS9406	Erik Brubaker	8132
1	MS9406	Craig Tewell	8132
2	MS9018	Central Technical Files	8944
2	MS0899	Technical Library	4536
1	MS0123	D. Chavez, LDRD Office	1011
1	MS0161	Patent and Licensing Office	11500


Sandia National Laboratories